Chemical Engineering Science 177 (2018) 245–260

Contents lists available at ScienceDirect

Chemical Engineering Science

journal homepage: www.elsevier.com/locate/ces

Intrusive measurements of air-water flow properties in highly turbulent supported plunging jets and effects of inflow jet conditions

Hang Wang [a,*], Nuryanto S. Slamet [a,b,1], Gangfu Zhang [a], Hubert Chanson [a]

[a] School of Civil Engineering, The University of Queensland, Brisbane, QLD 4072, Australia
[b] Research Center for Water Resources, Ministry of Public Works and Housing, Indonesia

HIGHLIGHTS

- Air-water flow measurements in supported plunging jets using large-size facility.
- Effects of jet length and impact velocity on air entrainment in plunging pool.
- Effects of jet disturbance levels on turbulent and air-water flow properties.
- Quantification of bubbly flow turbulence intensity using a total pressure sensor.

ARTICLE INFO

Article history:
Received 12 October 2017
Accepted 20 November 2017
Available online 23 November 2017

Keywords:
Plunging water jet
Air entrainment
Impact velocity
Jet length
Pre-aeration
Phase-detection probe
Total pressure
Two-phase flow turbulence intensity

ABSTRACT

A plunging jet is an efficient device to entrain gas into liquid flow. In many practical occasions, the gas entrainment needs to be carefully controlled, and the interaction between the shear flow turbulence and entrained bubbles has to be better understood. This paper presents a physical study of vertical supported two-dimensional plunging jets using a relatively large-size facility. The air-water flow and turbulence properties were measured with an intrusive phase-detection probe and a total pressure sensor simultaneously. The inflow pre-aeration and turbulence level of the falling jet were carefully characterised, and the effects of jet impact velocity and jet length on air entrainment in plunging pool were investigated. The experimental results were systematically compared to relevant studies. A discussion was developed on the quantification of turbulence intensity in highly-aerated flow based on total pressure measurement. The flow turbulence properties were derived respectively from the interfacial phase-detection signals and total pressure signals. The results highlighted difference in terms of the turbulence intensities between interfacial motions and water-phase turbulence. The present work showed that the jet impact velocity, jet length, inflow disturbance and pre-entrainment of air had considerable effects on air entrainment capacity and subsurface air-water flow properties in plunging jets hence should be carefully characterised in relevant studies.

1. Introduction

A plunging jet is the impingement of a rapid jet into a slower body of fluid. The occurrence of a plunging liquid jet is often accompanied by the entrainment of environmental gas at the intersection between the jet and the receiving bath, namely, along the impingement perimeter (Ervine et al., 1980). The flow in the downstream vicinity of the impingement point is a two-phase mixing flow with development of a turbulent shear layer (Thomas et al., 1983; Chanson, 1997). The intense turbulence and its interaction with the entrained gas bubbles enhance the mixing of fast and slow liquid fluids, as well as the mass and heat transfer between the gas and liquid phases (Chanson, 2009).

While a natural plunging jet flow such as a waterfall or a plunging wave is mostly an uncontrolled hydraulic phenomenon, an artificial plunging jet can be generated easily in a relatively stable manner and used as a device to facilitate fluid mixing in industrial processes, like in chemical reactors and water treatment plants (Bin, 1993; Kiger and Duncan, 2012). There are numerous occasions where the flow aeration associated with the jet impingement is beneficial (e.g. wastewater re-oxygenation, fish farming industry) or, contrarily, undesirable hence must be minimised (e.g. bottle filling, steel industry, nuclear reactor cooling system) (Kirchner,

* Corresponding author.
E-mail address: hang.wang@uqconnect.edu.au (H. Wang).
[1] Present address: School of Earth and Environmental Sciences, The University of Queensland, Brisbane, QLD 4072, Australia.

https://doi.org/10.1016/j.ces.2017.11.030
0009-2509/

1974; Van de Donk, 1981; Qu et al., 2011). Understanding the gas entrainment mechanisms, bubble diffusion processes and bubble-turbulence interplay is of fundamental importance for a safe and economical design/operation in these applications.

The most common plunging jets are water jets with free-surface open to air. Physical modelling and theoretical analysis demonstrated the critical role of the jet impact velocity on the onset of air entrainment and the air-water flow patterns underneath the impingement point (Sene, 1988; Bin, 1993). The jet disturbance is another key parameter, often linked with the jet length, local velocity turbulence and flow instabilities (Qu et al., 2011; Kiger and Duncan, 2012). While the air entrainment regimes were successfully investigated with high-speed flow visualisation (Chirichella et al., 2002), detailed characterisation of air-water flow properties in the plunging pool relied more upon intrusive phase-detection techniques (Serizawa et al., 1975; Brattberg and Chanson, 1998). Basic air-water flow properties that are of direct concern to engineering applications include void fraction, air entrainment rate, bubble size and penetration depth. These characteristics were well documented in literature for various types (circular/planar, laminar/turbulent) of jets (Lin and Donnelly, 1966; McKeogh and Ervine, 1981; Clanet and Lasheras, 1997; Cummings and Chanson, 1997a, 1997b; Chanson and Manasseh, 2003; Soh et al., 2005). The development in data processing and analysis in the past decade enabled further insight into the multiphase turbulence in terms of interfacial turbulence intensity, bubble clustering and integral turbulent length/time scales (Chanson and Carosi, 2007; Wang et al., 2014). Such measure of turbulence level in highly-aerated flow is difficult because of the presence of air bubbles, which not only limits the deployment of traditional monophase-flow measurement techniques, but also challenges the numerical modelling when the simulation results required verification against quantified bubble-turbulence interactions like bubble grouping and turbulence modification (Mudde, 2005). For plunging jet flows, there is lack of experimental study providing benchmark data on such detailed levels, and the current understanding on this highly-aerated, highly-turbulent flow is still vague.

To date, a number of studies demonstrated the impact of inflow turbulence on the inception conditions of air bubble entrainment (Ervine et al., 1980; Cummings and Chanson, 1999). Yet no study recorded quantitatively the impact of inflow turbulence levels on the two-phase flow properties for jet velocities substantially larger than the onset velocity. Herein the present study aimed to investigate the air-water flow properties in two-dimensional plunging jets and the processes of bubble advection and diffusion under the impact of intense turbulence. Physical experiments were performed using relatively large facilities and latest data analysis techniques. Systematic comparison was developed with particular focus on the effects of different inflow turbulence conditions of the jets upon the air entrainment and two-phase flow characteristics in the plunging pool. The effects of impact velocity and jet length were also tested for a range of flow conditions. The experimental results are presented in the order of jet pre-aeration and turbulence level, air-water flow properties in the plunging pool, two-phase turbulence properties in the plunging pool, and air entrainment rate.

2. Experimental setup and data processing

2.1. Experimental facility

The experimental setup was a two-dimensional vertical supported planar water jet. The apparatus consisted of a rectangular jet nozzle, a receiving water tank and the water supply system. Fig. 1 illustrates the experimental facility (Fig. 1a) and a detailed side-view sketch of the nozzle and the jet (Fig. 1b), where x, y, z are respectively the longitudinal, normal and transverse coordinates. Water was fed into the nozzle from a constant-head tank for discharges no greater than 0.0137 m^3/s and from a high-head pump for larger flow rates up to 0.038 m^3/s. The flow rates were measured respectively using an orifice meter and a Venturi meter in the feeding pipelines, with expected accuracy within ±2%, and the conservation of mass was checked for all experimental results. The rectangular nozzle was 0.269 m wide with a 0.012 m opening, discharging a quasi-two-dimensional planar jet into a large receiving tank. The free-falling jet was supported by a full-width PVC sheet extending from the nozzle edge into the receiving pool. The jet support was 0.35 m long, equipped with transparent sidewall windows to facilitate visual observation. The nozzle and the jet support were set at 88.5° from the horizontal to prevent jet detachment. The receiving tank was 2.5 m long, 1 m wide and 1.5 deep, built with a sharp-crest weir that allowed for a constant water level in the tank during the experiment (Fig. 1a). The large pool setup ensured that the air entrainment and diffusion processes in upper part of the pool were free of stagnation pressure or boundary friction effects of the tank walls.

The same jet nozzle was used in the previous work of Cummings and Chanson (1997a, 1997b, 1999), Brattberg and Chanson (1998) and Bertola et al. (2017). Table 1 summarises the respective flow conditions, along with remarks on the respective instrumentation, scanning rate and duration. Compared to the work in 1990s, the pipeline system and receiving tank were newly constructed, and the instruments had different sensor sizes. The sampling duration was substantially increased from less than 3 s to 90 s according to a sensitivity study. New data collection and processing techniques developed over the past two decades were adopted (Chanson and Carosi, 2007; Wang et al., 2014). The recent work of Bertola et al. (2017) was conducted using the same facility and instrumentation, except for a modified inflow condition in the present experiments linked to the installation of flow redistributors at upstream of the jet nozzle (Fig. 1b). The flow redistributors were a series of mesh rollers fitting in the pipe T-junction. They were introduced to reduce the three-dimensional flow instabilities noted by Bertola et al. (2017). The effects of the mesh rollers on jet turbulence modification and the consequential plunging jet air entrainment are discussed specifically in this paper.

2.2. Experimental instrumentation

The air-water flow properties were measured locally with an intrusive dual-tip phase-detection probe. The probe was equipped with two parallel needle sensors. Each needle sensor had a core electrode ($\varnothing$ = 0.25 mm) isolated from an outer electrode ($\varnothing$ = 0.8 mm). Bubbles were advected in the flow, and the air-water interfaces were detected by the sensor tip based on the change in electro-resistance between the core and outer electrodes when the sensor tip was in air or water phases (Crowe et al., 1998). The two sensors were aligned vertically against the jet flow direction, with a transverse separation Δz = 2 mm and a longitudinal distance Δx = 7.1 mm between the leading and trailing tips. Both sensors were sampled simultaneously at 20 kHz for 90 s at each measurement location. While the basic air-water flow properties such as the void fraction and bubble count rate were derived from the time series of the phase-detection probe signal, a correlation analysis of the signals of two sensors provided further turbulence properties including air-water interfacial velocity and turbulent length/time scales (Chanson and Carosi, 2007).

A miniature total pressure sensor was attached next to the phase-detection probe to measure the local instantaneous total pressure of the air-water flow. The pressure sensor had a 5 mm

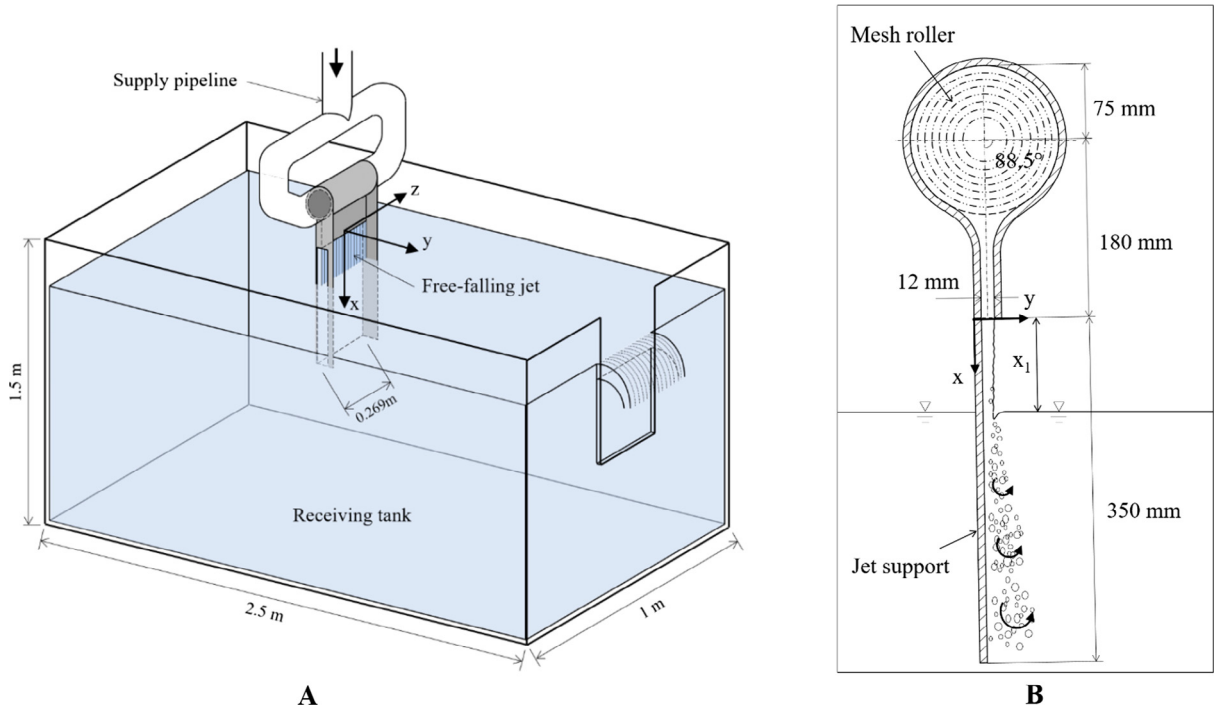

Fig. 1. Sketch of experimental facility: (A) general view of the jet nozzle and receiving tank; (B) Side view of the jet nozzle and support.

Table 1
Experimental flow conditions and instrumentation of present and previous studies.

	Q (L/s)	d_0 (m)	V_0 (m/s)	x_1 (m)	d_1 (m)	V_1 (m/s)	Instrumentation, scanning rate and scanning duration
Present study	7.1	0.012	2.20	0.05	--	2.4	Dual-tip phase-detection probe (∅0.25 mm, 20 kHz, 90 s)
	6.2	0.012	1.92	0.10	0.0092	2.4	Total pressure sensor (∅1 mm, 20 kHz, 90 s)
	5.4	0.012	1.67	0.15	--	2.4	
	11.1	0.012	3.42	0.05	0.0121	3.6	Dual-tip phase-detection probe (∅0.25 mm, 20 kHz, 90 s)
	11.0	0.012	3.40	0.10	0.0118	3.7	
	10.6	0.012	3.28	0.15	0.0101	3.7	
	17.8	0.012	5.51	0.05	0.0126	5.6	Dual-tip phase-detection probe (∅0.25 mm, 20 kHz, 90 s)
	17.2	0.012	5.33	0.10	0.0135	5.5	Total pressure sensor (∅1 mm, 20 kHz, 90 s)
	16.9	0.012	5.23	0.15	--	5.5	
Cummings and Chanson (1997a, 1997b)	6.46	0.012	2.01	0.0875	0.010	2.4	Single-tip phase-detection probe (∅0.35 mm, 40 kHz, 1 s)
	19.37	0.012	5.96	0.0875	0.0117	6.1	Dual-tip phase-detection probe (∅0.025 mm, 40 kHz, 1 s) Pitot tube (∅3.3 mm) & pressure transducer (500 Hz)
Brattberg and Chanson (1998)	4.61	0.012	1.43	0.10	0.0090	2.0	Dual-tip phase-detection probe (∅0.025 mm, 20–40 kHz, 3 s)
	8.56	0.012	2.65	0.10	0.0110	3.0	Pitot tube (∅3.3 mm) & pressure transducer (500 Hz)
	12.51	0.012	3.88	0.05	0.0118	4.0	Hot film probe (∅0.3 mm)
	12.10	0.012	3.75	0.10	0.0116	4.0	
	11.67	0.012	3.62	0.15	0.0114	4.0	
	15.49	0.012	4.80	0.10	0.0119	5.0	
	18.83	0.012	5.83	0.10	0.0120	6.0	
	22.14	0.012	6.86	0.10	0.0121	7.0	
	25.43	0.012	7.88	0.10	0.0121	8.0	
Bertola et al. (2017)	6.7	0.012	2.07	0.10	0.0105	2.5	Dual-tip phase-detection probe (∅0.25 mm, 20 kHz, 90 s)
	11.4	0.012	3.53	0.10	0.0115	3.8	Total pressure sensor (∅1 mm, 20 kHz, 90 s)
	17.4	0.012	5.42	0.10	0.0127	5.6	Pitot tube (∅3.2 mm)
	23.6	0.012	7.27	0.10	0.0127	7.4	Acoustic displacement meters (50 Hz, 180 s)

Notes: Q: flow rate; d_0: jet thickness at nozzle; V_0: jet velocity at nozzle; x_1: jet length; d_1: jet thickness at impingement point; V_1: impact velocity.

outer diameter and a 1 mm diameter silicon diaphragm on the sensor head, recording pressure variations based on the diaphragm mechanical deformation. It provided an absolute pressure measurement range from 0 to 1.5 bars, with a precision of 0.5%. Fig. 2 shows the side-by-side phase-detection probe and total pressure sensor. The pressure sensor head and the leading phase-detection sensor tip were at the same longitudinal (vertical) and normal (horizontal, perpendicular to the jet support) positions, the centres being separated by $\Delta z = 6.2$ mm in the transverse direction. The same scanning rate (20 kHz) and duration (90 s) were applied for the pressure sensor.

Moving in the x-y plane on the jet centreline (see Fig. 1b), the relative positions of the probes to the plunging jet were controlled by two fine-adjustment travelling mechanisms in the longitudinal and normal directions. The probe positions were read out of digital positioning scales with errors less than 0.1 mm in each direction.

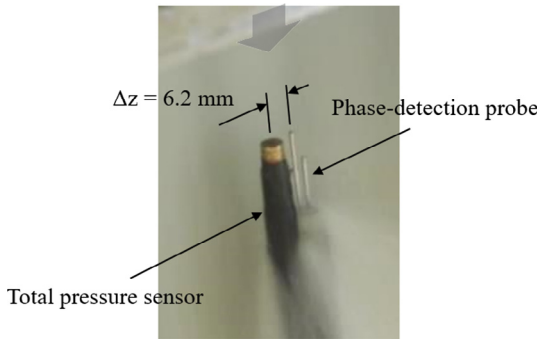

Fig. 2. Dual-tip phase-detection probe and total pressure sensor in vertical jet. Thick arrow shows the flow direction.

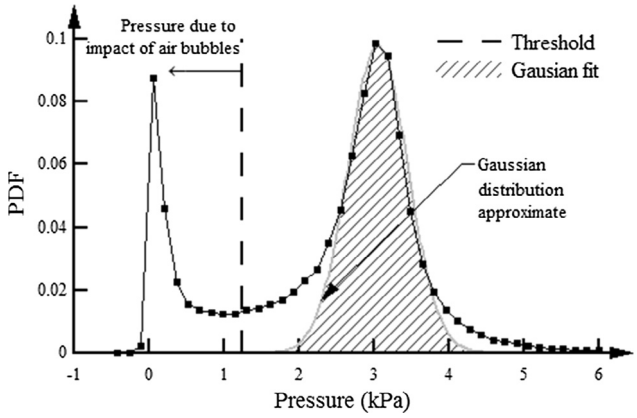

Fig. 3. Probability density function of total pressure samples in aerated free-falling jet – V_0 = 2.07 m/s, x = 0.1 m, y = 0.007 m; C = 0.12, F = 38.8 Hz.

2.3. Data processing: turbulence intensities in aerated flow

Basic air-water flow properties were measured on the phase-detection probe leading tip and analysed based on binarised instantaneous void fraction samples which were 0 for water and 1 for air. A 50% threshold between the maximum air and water probabilities was adopted for the signal binarisation (Toombes, 2002). The simultaneous scanning of dual-tip probe sensors provided further the time-averaged velocity of air-water interfaces travelling in the longitudinal direction:

$$V_{int} = \frac{\Delta x}{T_{int}} \quad (1)$$

where Δx is the longitudinal separation distance between the two phase-detection probe sensor tips, and T_{int} is average interfacial travel time over the distance Δx. Denoting $R_{xy}(\tau)$ as the cross-correlation function between the signals of two phase-detection sensors and $(R_{xy})_{max}$ the maximum cross-correlation coefficient, T_{int} equals to the time lag of $(R_{xy})_{max}$, i.e. $R_{xy}(\tau = T_{int}) = (R_{xy})_{max}$.

The turbulent fluctuations in air-water interfacial velocity were approximated based on the shapes of the auto-correlation function $R_{xx}(\tau)$ and cross-correlation function $R_{xy}(\tau)$. Assuming a random detection of an infinitely large number of air-water interfaces by the phase-detection sensors, the correlation functions of the signal followed a Gaussian distribution, and the interfacial turbulence intensity Tu_{int} was calculated as (Felder and Chanson, 2014)

$$Tu_{int} = \frac{v'}{V_{int}} = \frac{1}{T_{int}}\sqrt{\frac{2}{\pi}\left(\left(\frac{T_{xy}}{(R_{xy})_{max}}\right)^2 - T_{xx}^2\right)} \quad (2)$$

where Tu_{int} is the interfacial turbulence intensity, V_{int} is the local time-averaged interfacial velocity, v'_{int} is the velocity standard deviation, and T_{xx} and T_{xy} are respectively the auto- and cross-correlation time scales defined as

$$T_{xx} = \int_0^{\tau(R_{xx}=0)} R_{xx}(\tau)d\tau \quad (3)$$

$$T_{xy} = \int_T^{\tau(R_{xy}=0)} R_{xy}(\tau)d\tau \quad (4)$$

In a highly-aerated turbulent flow, the interfacial velocity fluctuations often differ from the water-phase turbulence. The quantification of the latter may be derived from a total pressure measurement, albeit this is not straightforward because of the presence of air bubbles. That is, the total pressure signal in a bubbly flow contained pressure drops corresponding to the impact of air bubbles on the pressure sensor. Fig. 3 shows a typical probability density function (PDF) of total pressure signal in the aerated jet (C = 0.12), where the bimodal PDF distribution reflected the water-phase total pressure fluctuation around a mean value of 3.02 kPa (relative to atmospheric pressure) and a significant amount of pressure drop to 0.05 kPa due to the air bubble impact. Zhang et al. (2016) developed an approximate approach to the water-phase turbulence intensity in air-water flow based on the fluctuations in total pressure:

$$Tu_w = \sqrt{\frac{\frac{p_t'^2}{\rho_w^2 V_w^4} - \frac{(1-\alpha)\alpha}{4}}{(1-\alpha)(1+\frac{\alpha}{2})}} \quad (5)$$

where Tu_w is the turbulence intensity of the water phase, p_t' is the total pressure standard deviation, ρ_w is the water density, V_w is the local time-averaged water-phase velocity and α is the percentage of total pressure samples affected by air bubbles. The water-phase turbulence intensity was obtained by eliminating the effects of air bubbles which was interpreted in Zhang et al. (2016) in terms of $\alpha = C$, C being the time-averaged void fraction measured by phase-detection probes. However, because of the different geometries and response mechanisms of the total pressure and phase-detection sensors, the void fraction often mis-predicted the percentage of bubble-affected pressure drops in a bubbly flow, i.e. $\alpha \neq C$.

In the present work, two approaches were attempted to achieve a more physical estimate of Tu_w. Approach I was to determine α directly from the total pressure signal by applying a single 40% threshold between the two PDF peaks (Fig. 3), with α being the number of pressure sample points below the threshold divided by the total number of pressure samples. Approach II, on the other hand, assumed a Gaussian distribution for the PDF of instantaneous water-phase total pressure, as illustrated in Fig. 3. After removing the bubble-affected pressure samples below the threshold, as described in Approach I, a Gaussian distribution was fitted against the remaining PDF, and the standard deviation $(p_t')_w$ was obtained for the water phase, and Eq. (5) became:

$$Tu_w = \sqrt{\frac{(p_t')_w^2}{\rho_w^2 V_w^4}} \quad (6)$$

with $(p_t')_w < p_t'$ and $\alpha = 0$. Note that Eqs. (5) and (6) neglected the higher order terms Tu_w^3, Tu_w^4 (Zhang et al., 2016). Further, the use of water velocity and interfacial velocity made little difference in high-speed bubbly flow where the non-slip condition applied, i.e. $V_w \approx V_{int}$.

2.4. Experimental flow conditions

All measurements were conducted on the jet centreline at several cross-sections perpendicular to the jet support. Three jet impact velocities were investigated: V_1 = 2.4, 3.7 and 5.5 m/s. Here V_1 is the cross-sectional average jet velocity at the longitudinal position of the impingement point ($x = x_1$). For each impact velocity, three impingement positions were tested: x_1 = 0.05, 0.1 and 0.15 m, corresponding to three jet lengths denoted x_1 for simplicity. The flow conditions are summarised in Table 1, where the jet thickness at impact d_1 was the equivalent clear water depth deriving from phase-detection probe measurements at $x = x_1$. The equivalent clear water depth was close to the theoretical jet thickness given by the continuity and Bernoulli equations based on nozzle opening d_0, nozzle velocity V_0 and jet length x_1.

3. Free-falling jet: pre-aeration and inflow turbulence

3.1. Air entrainment in free-falling jet

The free-falling jet was quasi-two-dimensional. The nozzle edge induced a flow singularity at ($x = 0$, $y = d_0$), and an interfacial air-water mixing layer developed downstream at the jet free-surface. The air entrainment through the jet surface is referred to herein as the jet pre-aeration, with respect to the singular air entrainment at the impingement point. The pre-aeration was expected to be driven by both jet surface disturbance originating from the nozzle edge and the flow turbulence that interacted with the free-surface (Hoyt and Taylor, 1977; Chanson, 1997).

Herein the jet pre-aeration was quantified using the phase-detection probe on the jet centreline. Typical void fraction distributions are shown in Fig. 4a for a given nozzle velocity V_0 = 5.3 m/s. The results are compared with a previous dataset by Bertola et al. (2017) in terms of the air entrainment ratio (Fig. 4b), air diffusion layer thickness (Fig. 4c) and maximum bubble count rate (Fig. 4d). The comparison showed similar streamwise variation trends for all parameters between the present and previous studies, while the effects of inflow turbulence modification can be seen, associated with the installation of mesh rollers in the upstream pipeline (Fig. 1b). Compared to the earlier work without the mesh rollers, a better-organised flow was delivered into the nozzle, with a more uniform flow and less free-surface disturbance in the falling jet, as well as potentially modified turbulence levels.

The void fraction distributions showed almost clear water with little air entrainment immediately downstream of the nozzle, followed by a rapid increase in the amount of entrained air along the jet (Fig. 4a and b). In Fig. 4a, the void fraction profiles are compared with the theoretical solution of the advective diffusion equation for air bubbles in a high-velocity water jet discharging into air (Chanson, 1997):

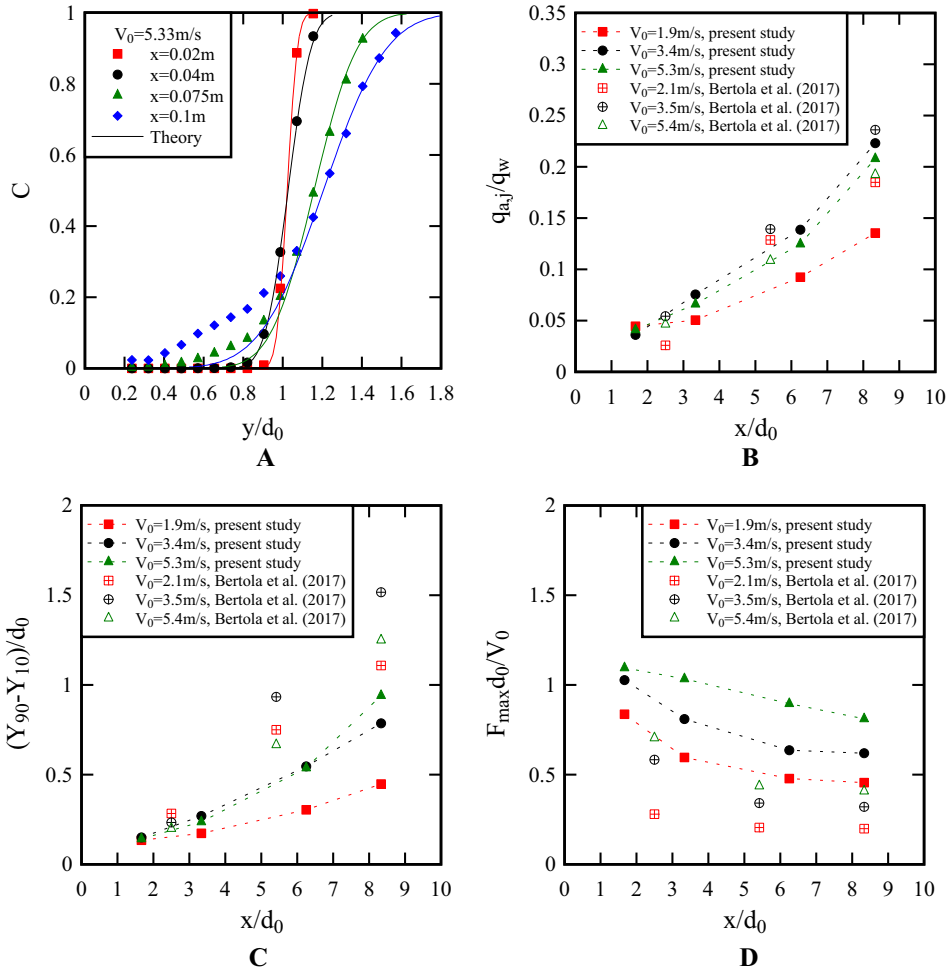

Fig. 4. Air entrainment in free-falling jet: (A) Void fraction distributions at different cross-sections on jet centreline – V_0 = 5.8 m/s; (B) Ratio of air entrainment to water discharge – comparison with data of Bertola et al. (2017) at x = 0.1 m; (C) Longitudinal development of air diffusion layer thickness at jet free-surface – comparison with data of Bertola et al. (2017); (D) Longitudinal development of maximum bubble count rate near the jet free-surface – comparison with data of Bertola et al. (2017).

$$C = \frac{1}{2}\left(1 + \mathrm{erf}\left(\frac{y - Y_{50}}{\sqrt{D_t \frac{x}{V}}}\right)\right) + \frac{1}{2}\left(1 - \mathrm{erf}\left(\frac{y + Y_{50}}{\sqrt{D_t \frac{x}{V}}}\right)\right) \quad (7)$$

where D_t is a depth-averaged diffusivity, Y_{50} is the location where C = 0.5, V is the free-stream velocity and erf() is the Gaussian error function. Eq. (7) describes a typical interfacial self-aeration process, which agreed well with the present experimental data for $x/d_0 < 6$, and for $x/d_0 > 6$ when $y > Y_{50}$. For $x/d_0 > 6$, $y < Y_{50}$, the experimental data showed higher void fraction than the theoretical prediction. Similar findings were reported in Bertola et al. (2017) for large jet velocities with even higher air content next to the jet support. The difference between the physical data and theoretical expression suggested additional sources of air entrainment other than the free-surface aeration. Considering the initial clear-water jet condition at the nozzle, the additional air entrainment was most likely caused by the presence of unsteady three-dimensional structures in the jet. Such disturbance structures developed along the jet and changed positions randomly in the spanwise direction, sometimes leading to air cavities between the jet flow and the support wall. This may also explain the void fraction and bubble count rate distributions in the plunging pool, with a secondary peak next to the jet support corresponding to the secondary air entrainment source (see Section 4.1). The jet disturbance and associated flow instabilities were reduced in the present study by introducing the flow redistributors upstream of the nozzle, and the difference from the earlier work of Bertola et al. (2017) can be seen in terms of interfacial turbulence intensity and auto-correlation time scale in Sections 5.2 and 5.3.

Fig. 4b shows the longitudinal increase in air entrainment rate for different jet velocities. Herein the jet air entrainment flux $q_{a,j}$ was calculated as

$$q_{a,j} = \int_0^d CV dy \quad (8)$$

where d is the jet thickness, $d = Y_{50}$ in the present study. The data are compared with Bertola et al. (2017) for similar jet velocities, where d was set to be the equivalent clear water depth that was found close to Y_{50}. The results showed comparable pre-entrainment ratios $q_{a,j}/q_w$ at the impingement point between 13% and 24% for both experiments. Visually a more uniform surface roughness pattern was observed in the present study, with smaller jet disturbance and less flow instabilities. This was consistent with the smaller thickness of surface air-water mixing layer $(Y_{90} - Y_{10})/d_0$ for the present setup, as shown in Fig. 4c, where Y_{90} and Y_{10} are locations with C = 0.9 and 0.1 respectively. Nevertheless, the broadening of the surface mixing layer over the 0.1 m jet length was considerable, characterising a relatively high jet surface disturbance. In a given cross-section, the maximum bubble count rate F_{max} was consistently observed at a position close to the jet surface where the void fraction C = 0.5. The results were overall consistent with the literature on pure free-surface aeration in planar jets discharging into air (Low, 1986; Brattberg et al., 1998). The dimensionless maximum bubble count rate $F_{max}d_0/V_0$ increased with increasing jet velocity and, for a given velocity, decreased along the falling jet (Fig. 4d). Compared to the setup in Bertola et al. (2017), a larger number of bubbles (or water-air interfaces) were induced as a result of the turbulence modification and free-surface breaking. Considering the comparable pre-entrainment air fluxes in both studies, the higher bubble or interface count rate (Fig. 4d) could indicate entrainment of smaller air bubbles, or higher jet surface fluctuation rate detected by the fixed phase-detection sensor.

3.2. Turbulence intensity in pre-aerated jet

Velocity measurements in the falling jet showed negligible boundary layer development against the jet support. The free-stream turbulence intensity was estimated using Eqs. (5) and (6). The results given by both approaches are summarised in Table 2 for the present study and Bertola et al. (2017), where the listed values are the average turbulence intensities for $0.5 < y/d_1 < 0.8$ at x = 0.1 m. The reference data of Cummings and Chanson (1997a) and Brattberg and Chanson (1998) in Table 2 were obtained with different methods (but with the same nozzle), the former using a Pitot tube connecting to a pressure transducer and the latter using a hot-film probe.

The two approaches yielded similar results with the same order of magnitude. The jet flows in the present study had slightly larger free-stream turbulence intensities than in Bertola et al. (2017), linked to the presence of additional flow redistributors in the inflow pipe. The higher turbulence intensity might be responsible for the higher bubble count rate in the pre-aerated jets (Fig. 4d). Both studies using the current facilities had more turbulent jets than the experiments in 1990s. The effects of jet velocity on jet turbulence intensity were not obvious. For a given velocity, the present study and Brattberg and Chanson (1998) showed consistently a larger turbulence intensity for a longer jet length.

Table 2
Turbulence intensity in aerated free-falling jet prior to impingement.

	q_w (m^2/s)	V_1 (m/s)	x_1 (m)	Tu_w Approach I (Eq. (5))	Tu_w Approach II (Eq. (6))
Present study	0.0264	2.4	0.05	0.052	0.058
	0.0230	2.4	0.1	0.111	0.084
	0.0662	5.6	0.05	0.058	0.091
	0.0639	5.5	0.1	0.045	0.146
Bertola et al. (2017)	0.0249	2.5	0.1	0.087	0.056
	0.0424	3.8	0.1	0.041	0.059
	0.0647	5.6	0.1	0.039	0.044
	0.0877	7.4	0.1	0.017	0.042
Cummings and Chanson (1997a, 1997b)	0.0240	2.39	0.0875	0.016	
	0.0720	6.14	0.0875	0.0075	
Brattberg and Chanson (1998)	0.0171	2.0	0.1	0.0173	
	0.0318	3.0	0.1	0.0265	
	0.0465	4.0	0.05	0.02	
	0.0450	4.0	0.1	0.0285	
	0.0434	4.0	0.15	0.03	
	0.0576	5.0	0.1	0.025	

Notes: q_w: water discharge per unit width; V_1: impact velocity; x_1: jet length; Tu_w: turbulence intensity deriving from total pressure measurement.

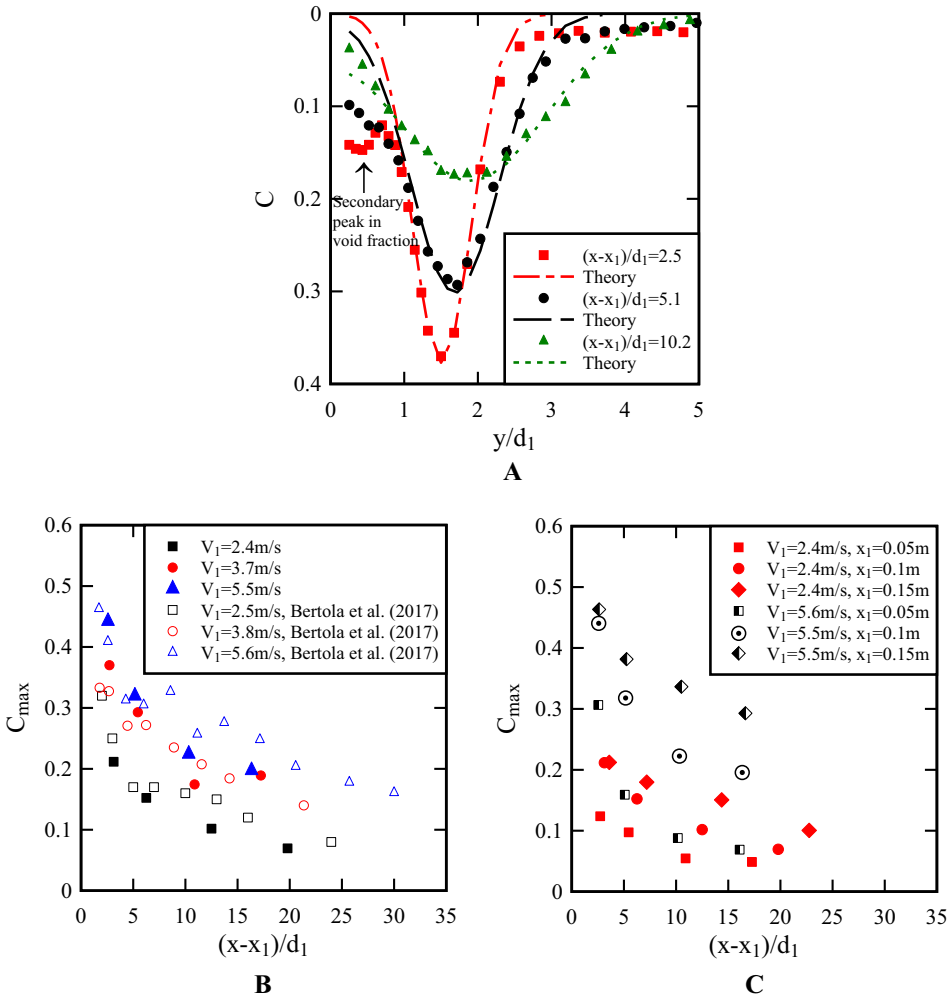

Fig. 5. Time-averaged void fraction in plunging jets: (A) Typical void fraction distributions with comparison to Eq. (5) – V_1 = 3.7 m/s, x_1 = 0.1 m; (B) Longitudinal decay of maximum void fraction – Effect of impinging velocity, x_1 = 0.1 m; (C) Longitudinal decay of maximum void fraction – Effect of jet length.

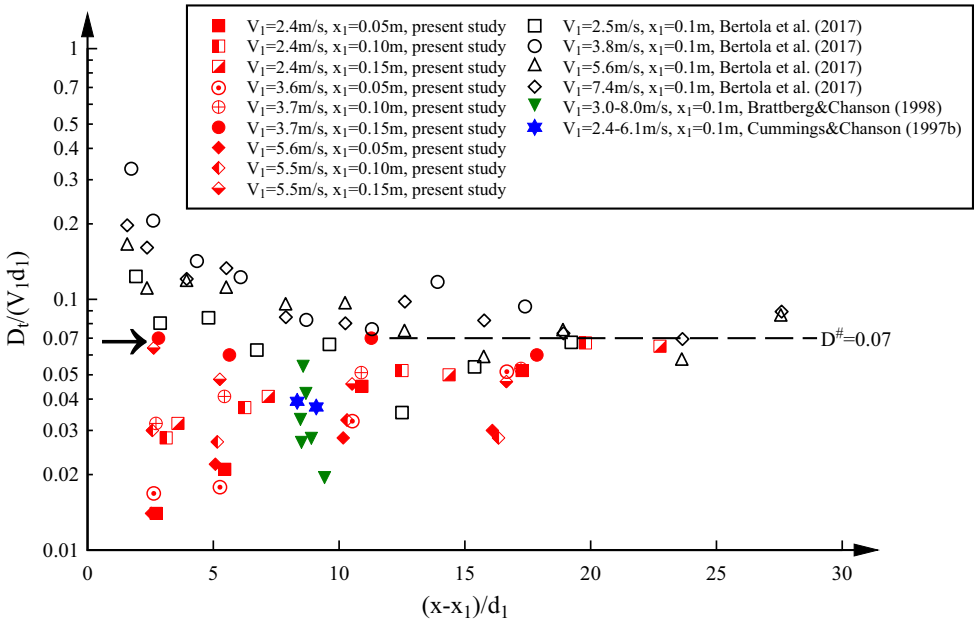

Fig. 6. Longitudinal variation of dimensionless diffusivity in air diffusion layer. Arrow indicates data sets with highly disturbing jet conditions and large diffusivity at impingement.

4. Plunging jet: air-water flow properties

For all investigated flow conditions (2.4 m/s < V_1 < 5.6 m/s, 0.05 m < x_1 < 0.15 m), a bubble cloud formed underneath the impingement point, and the penetration depth increased with increasing impact velocity V_1. Visible vortical structures formed and were advected in the shear layer (Fig. 1b), carrying entrained bubbles into deep water. Both the entrainment of air and successive formation of large vortices appeared to contribute to free-surface fluctuations in the receiving pool, leading to an instantaneous change in jet length and oscillations of impingement point elevation around a mean position x_1. Some entrained bubbles were dispersed in water, while the rest were driven back to the free-surface by buoyancy or re-entrained into the shear layer by recirculating flow motions. Basic air-water flow properties were measured on the phase-detection probe leading tip, including the time-averaged void fraction, bubble count rate and bubble chord length.

4.1. Void fraction

Fig. 5a presents typical distributions of time-averaged void fraction C in the downstream vicinity of impingement point for V_1 = 3.7 m/s, x_1 = 0.1 m, at three depths. The void fraction profile exhibited a marked maximum C_{max} at a horizontal position Y_{Cmax}. The maximum void fraction decreased with increasing depth below the impingement point. Fig. 5b plots the longitudinal decay of maximum void fraction for various impact velocities with the same jet length x_1 = 0.1 m. The effects of jet length are illustrated in Fig. 5c for two velocities.

In Fig. 5a, a secondary peak was seen in the first cross-section ($(x - x_1)/d_1$ = 2.5, i.e. $x - x_1$ = 0.02 m) between y = 0 and Y_{Cmax}. This local peak void fraction corresponded to the extra air entrainment next to the jet support, associated with the interaction between some three-dimensional jet disturbance structures and the support wall, which had allowed air in between the jet and the wall. This was a unique type of jet pre-aeration observed for supported jets with relatively long falling lengths and high developing disturbance. The void fraction profile was the superposition of this pre-aeration and the analytical solution of bubble diffusion equation with a point source of air bubbles at $x = x_1$, $y = d_1$ (Chanson, 1997):

$$C = \frac{q_a}{q_w} \frac{\frac{Y_{Cmax}}{d_1}}{\sqrt{4\pi D^{\#} \frac{x-x_1}{d_1}}} \left(\exp\left(-\frac{1}{4D^{\#}} \frac{\left(\frac{y-Y_{Cmax}}{d_1}\right)^2}{\frac{x-x_1}{d_1}} \right) + \exp\left(-\frac{1}{4D^{\#}} \frac{\left(\frac{y+Y_{Cmax}}{d_1}\right)^2}{\frac{x-x_1}{d_1}} \right) \right) \quad (9)$$

where q_a is the air flow rate per unit width in the plunging pool and $D^{\#}$ is a dimensionless diffusivity assumed independent of the

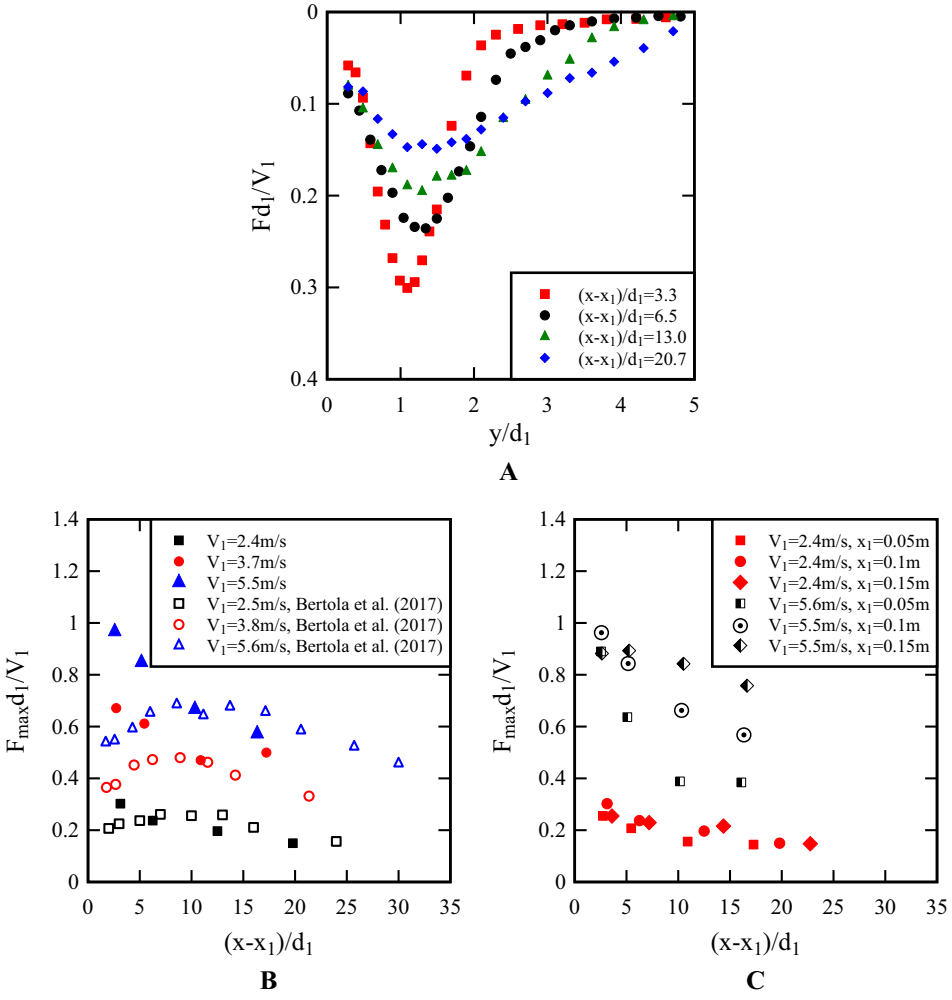

Fig. 7. Bubble count rate in plunging jets: (A) Typical distributions of dimensionless bubble count rate – V_1 = 2.4 m/s, x_1 = 0.1 m; (B) Longitudinal variation of maximum bubble count rate – Effect of impinging velocity, x_1 = 0.1 m; (C) Longitudinal variation of maximum bubble count rate – Effect of jet length.

horizontal position: $D^{\#} = D_t/(V_1 d_1)$. Eq. (9) is compared with the experimental data in Fig. 5a, the agreement indicating the bubble transport in the subsurface bubbly flow being primarily an advective diffusion process. The magnitude of maximum void fraction and the rate of its longitudinal decay were shown mostly consistent between the present data and the data of Bertola et al. (2017) for similar impact velocities (Fig. 5b). Although Eq. (9) implied a relationship $C_{max} \propto (x - x_1)^{-0.5}$, a range of exponents between −0.35 and −0.6 were reported in the literature (e.g. Brattberg and Chanson, 1998). Fig. 5b shows that a larger impact velocity led to a larger maximum void fraction C_{max} that decayed over a longer longitudinal distance. This was consistent with the observation of

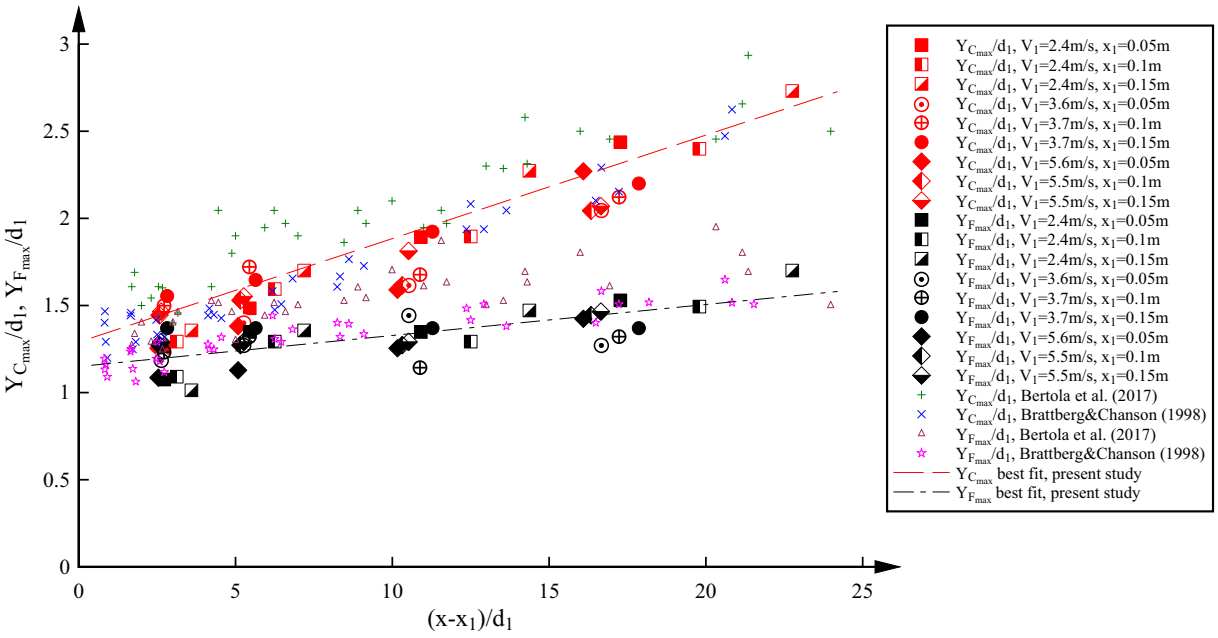

Fig. 8. Positions of maximum void fraction and maximum bubble count rate as functions of longitudinal position – Comparison with linear fits and previous data of Brattberg and Chanson (1998) and Bertola et al. (2017).

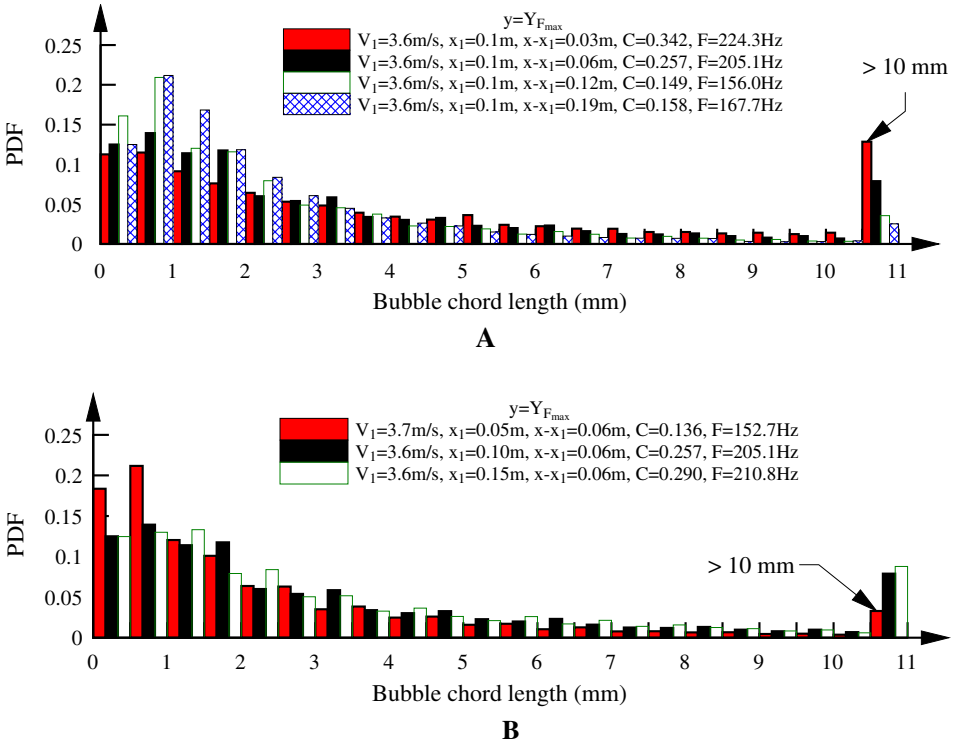

Fig. 9. Probability distributions of bubble chord length at the position of maximum bubble count rate: (A) Longitudinal variation of bubble chord length probability distribution in the same plunging jet (V_1 = 3.6 m/s, x_1 = 0.1 m); (B) Bubble chord length probability distributions at the same distance below impingement point for different jet lengths (x_1 = 0.05 m, 0.1 m & 0.15 m).

more intense air entrainment and a larger bubble penetration depth for a faster impinging jet. Similar effects of a longer jet length are shown in Fig. 5c.

The diffusivity coefficient $D^{\#}$ was derived from the best fit of Eq. (9) to the experimental data. The results are plotted in Fig. 6 as a function of the longitudinal position, with comparison to the findings of Cummings and Chanson (1997b), Brattberg and Chanson (1998) and Bertola et al. (2017). The present data yielded $0.01 < D^{\#} < 0.07$, agreeable with those of Cummings and Chanson (1997b) and Brattberg and Chanson (1998). For most flow conditions, the data showed an increasing trend in the longitudinal direction as the diffusion layer expanded. Although the data of Bertola et al. (2017) approached the same dimensionless value $D^{\#} \sim 0.07$ downstream (Fig. 6), large diffusivities were obtained close to the impingement point, showing a decreasing trend for $0 < x - x_1 < 10d_1$. The decreasing trend was also observed for two of the present jet conditions, namely, $V_1 = 3.7$ and 5.5 m/s with the largest jet length $x_1 = 0.15$ m (see the arrow in Fig. 6). This relatively high diffusivity in the vicinity of impingement point was linked to the high jet disturbance and surface breaking that resulted in a thickened air-water mixing layer below the impingement point. The impact of the disturbance on the subsurface bubble distribution was only seen within a short distance ($\sim 10d_1$) below the impingement point. Note that the jet disturbance level was reduced in the present study, compared to that in Bertola et al. (2017). As a result, only the most disturbing inflow conditions in the present experiments were under the impact of large jet disturbance thus showing a decreasing $D^{\#}$, whereas the same effects were seen for all flow conditions in Bertola et al. (2017), even with the lowest jet velocity. For a given impact velocity, a larger jet length allowed for more developed jet disturbance hence yielded larger diffusivity coefficients in the plunging pool.

4.2. Bubble count rate

The bubble count rate is the number of bubbles detected by one phase-detection sensor per second. For a given void fraction, the bubble count rate is proportional to the total interfacial area between entrained air and surrounding water, thus relevant to the air-water mass transfer. Several studies on air-water shear flow showed strong coupling between bubble count rate and local shear force as well as the flow Reynolds number (e.g. Wang and Chanson,

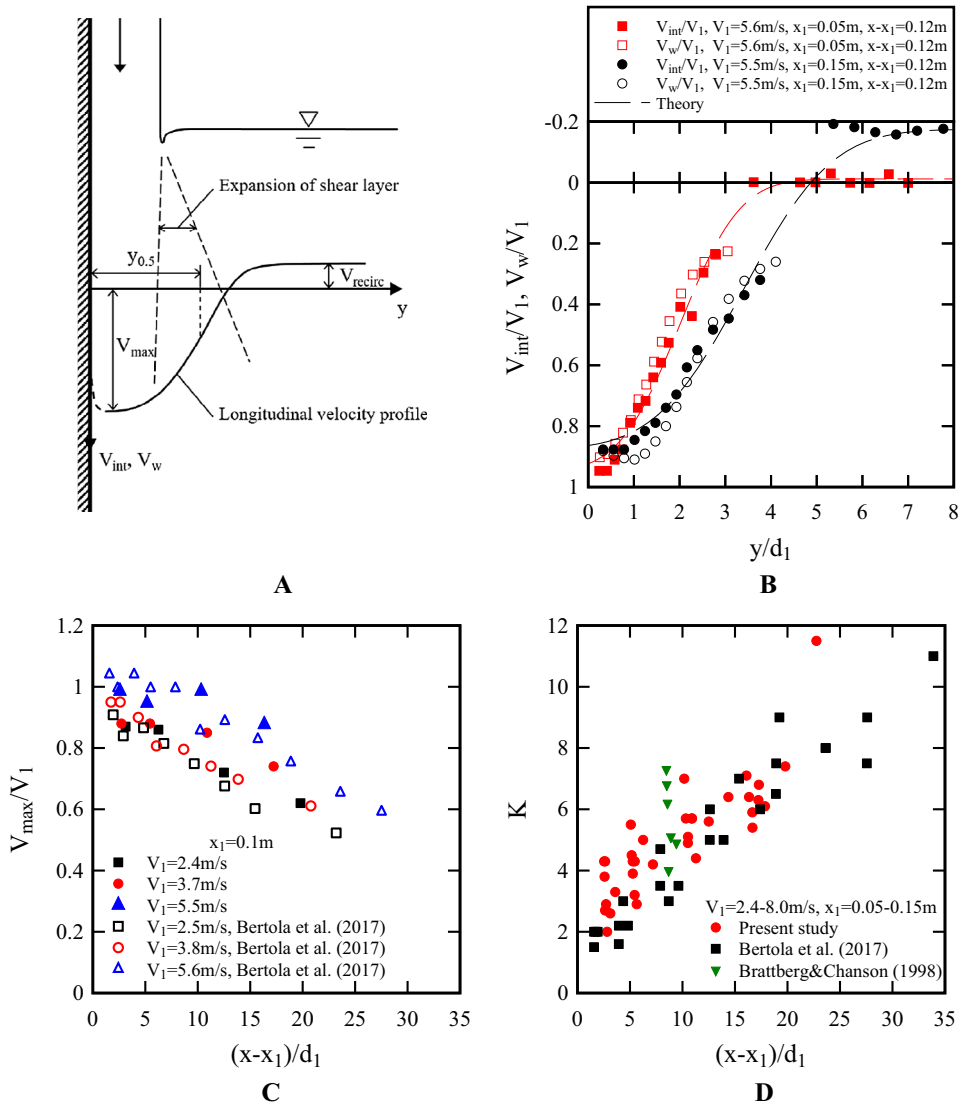

Fig. 10. Time-averaged longitudinal interfacial velocity: (A) Definition sketch; (B) Typical longitudinal interfacial velocity distributions, with comparison to Eq. (12) and total pressure measurement; (C) Longitudinal decay of maximum velocity, with comparison to data of Bertola et al. (2017); (D) Longitudinal variation of coefficient K in Eq. (12), with comparison to data of Brattberg and Chanson (1998) and Bertola et al. (2017).

2016). Fig. 7 presents the typical unimodal distributions of dimensionless bubble count rate in the plunging jet (Fig. 7a) and the longitudinal variation of the maximum value $F_{max}d_1/V_1$ (Fig. 7b and c). The presence of the maximum bubble count rate corresponded to the singular air entrainment at the impingement point and the most intense interplay between the entrained bubbles and local shear stresses, during which large air packets were broken into small particles. For a large impact velocity and jet length, a secondary local maximum was also seen between the dominant peak and the support wall, in consistence with the above discussion for the void fraction data.

The present data showed monotonically decreasing maximum bubble count rate with increasing depth (Fig. 7b and c). The data were agreeable with previous experiments using the same sensor size for $x - x_1 > 8d_1$ (Bertola et al., 2017). For $0 < x - x_1 < 8d_1$, however, the previous experimental results showed smaller maximum bubble count rates, with an overall pseudo-parabolic profile shape for the longitudinal evolution of F_{max} (Fig. 7b) (Brattberg and Chanson, 1998; Bertola et al., 2017). The high initial maximum bubble count rate in the present study was associated with the high interface count rate in the free-falling jets (Fig. 5d). Basically, the present impinging jets were more breaking due to the installation of in-pipe mesh rollers. The breaking jet surface and associated generation of splashing drops entrained a larger number of small bubbles at the jet impingement. These small air particles had low momentum and were detrained rapidly over a short distance below the pool free-surface. For comparison, the dominant processes in the previous experiments with less breaking jets were the entrapment of large air packets and their breakup into small bubbles by the shear forces, thus yielding a streamwise increasing F_{max} for $0 < x - x_1 < 8d_1$. A larger impact velocity gave a larger maximum bubble count rate at a given cross-section. While the effects of jet length were not obvious for a small impact velocity (e.g. $V_1 = 2.4$ m/s in Fig. 7c), a larger bubble count rate was observed, along with a lower longitudinal decay rate, for a relatively high impact velocity (e.g. $V_1 = 5.5$–5.6 m/s in Fig. 7c).

The presence of maximum void fraction C_{max} and maximum bubble count rate F_{max} were respectively related to the development of an air diffusion layer and turbulent shear layer (Chanson, 1997). The respective horizontal positions Y_{Cmax} and Y_{Fmax} did not coincide. Fig. 8 plots the position data for all tested flow conditions. The present data were best fitted by

$$\frac{Y_{C_{max}}}{d_1} = 0.0594\left(\frac{x - x_1}{d_1}\right) + 1.19 \quad (10)$$

$$\frac{Y_{F_{max}}}{d_1} = 0.0178\left(\frac{x - x_1}{d_1}\right) + 1.15 \quad (11)$$

A comparison with Brattberg and Chanson (1998) and Bertola et al. (2017) showed good agreement of the present data with the former and slightly larger Y_{Cmax} and Y_{Fmax} recorded by the latter. Note that simplistic linear fits like Eqs. (10) and (11) originated the diffusion layer and the shear layer at $1.15 < y/d_1 < 1.2$, rather than $y = d_1$. This can be understood by noting that d_1 was the equivalent clear water depth, while, for a highly aerated free-falling jet, the thickness of air-water mixing layer at the jet surface should not be ignored.

4.3. Bubble chord length

The bubble size distributions may be characterised in terms of the bubble chord length which is the time of a bubble spent on the phase-detection probe tip multiplied by the local velocity (velocity data are presented in Section 5.1). Fig. 9 shows the PDFs of bubble chord length measured at $y = Y_{Fmax}$ in given cross-sections. Fig. 9a shows the results at four cross-sections in the same plunging jet ($V_1 = 3.6$ m/s, $x_1 = 0.1$ m), and Fig. 9b demonstrates the effect of jet length for three jets with similar impact velocity, all at $x\text{-}x_1 = 0.06$ m. For all data sets, the bin size of PDF was 0.5 mm, and all data greater than 10 mm were re-grouped at the end of axis.

The results showed a broad bubble chord length spectrum from sub-millimetres to centimetres. The probability distribution skewed towards small bubble size, with the largest population mostly between 0.5 and 1 mm. As the depth increased, the percentage of sub-millimetric bubbles increased and that of large air packets (>10 mm) decreased (Fig. 9a), indicating a longitudinal decrease in mean bubble size. Noting meanwhile the longitudinal decrease in bubble count rate (Section 4.2), this implied a de-aeration of the two-phase receiving flow with increasing depth. In addition to the breakup of large bubbles during their advection in the shear flow, the decrease in mean bubble size was also contributed by the development of large-scale vortical structures. Large bubbles were captured in these vortical structures, some were ejected into ambient water by centrifugal force, and some were recirculated back into the high-momentum region and experienced further break-up process. For an elongated jet length, a greater proportion of large bubbles were detected at the same distance below the pool free-surface (Fig. 9b).

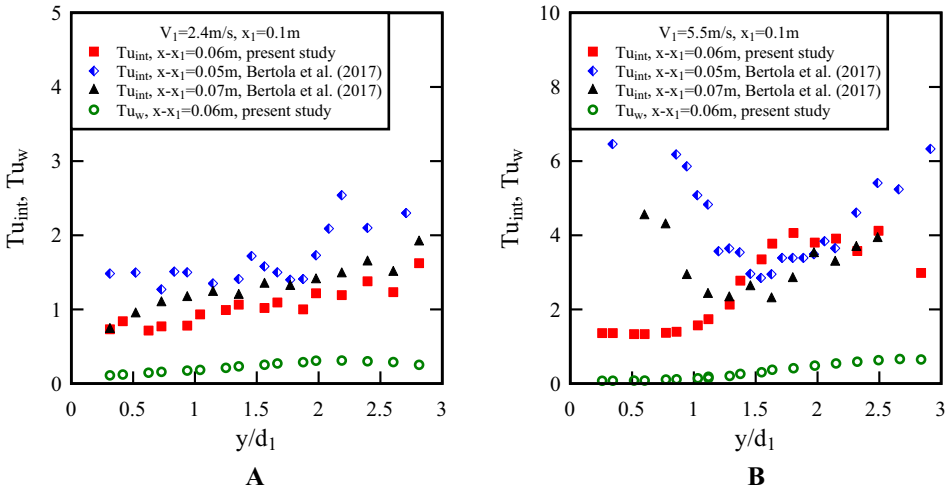

Fig. 11. Turbulence intensities for air-water interface and water-phase fluid underneath the impinging jet – Comparison with interfacial turbulence intensity data of Bertola et al. (2017): (A) $V_1 = 2.4$ m/s, $x_1 = 0.1$ m; (B) $V_1 = 5.5$ m/s, $x_1 = 0.1$ m.

5. Plunging jet: velocity and turbulence

The use of dual-tip phase-detection probe provided some measure of air-water flow turbulence properties by correlating the two sensor signals. These properties included the time-averaged longitudinal velocity V_{int}, turbulence intensity Tu_{int} and auto-correlation time scale $T_{xx,int}$, the subscript int denoting the properties of air-water interfaces, which may differ from the liquid-phase turbulence properties when the compressibility of air is not negligible or the non-slip condition is no longer valid (e.g. when the flow velocity is small). The total pressure sensor responded directly to the velocity fluctuations in the flow, although the signal encompassed low-pressure samples associated with the impact of air bubbles. Herein the velocity, turbulence intensity and auto-correlation time scale were also derived from the total pressure signals, denoted as V_w, Tu_w and $T_{xx,p}$. Comparison between the results of two instruments is presented.

5.1. Time-averaged velocity

The time-averaged interfacial velocity V_{int} was calculated using Eq. (1). Fig. 10a shows a definition sketch of typical velocity profile in the plunging pool. Fig. 10b presents the experimental results in two plunging jets with similar impact velocities but different jet lengths, where the velocity profiles were measured at the same depth beneath the impingement point. The velocity profiles showed the transition from high-speed flow next to the jet support to the still surrounding water. Large velocity gradient was observed immediately below the impingement point, followed by a gradual broadening of the shear layer with less sharp velocity transition further downstream. The velocity distributions followed the analytical solution of the equation of motion in a free shear layer (Rajaratnam, 1976; Schlichting, 1979). A modified form was proposed herein to take into account the upward flow reversal:

$$\frac{V_{int} - V_{recirc}}{V_{max} - V_{recirc}} = \frac{1}{2}\left(1 - \text{erf}\left(\frac{K(y - y_{0.5})}{x - x_1}\right)\right) \quad (12)$$

where V_{recirc} is the mean recirculation velocity, V_{max} is the maximum streamwise velocity, $y_{0.5}$ is the horizontal position where $V_{int} = (V_{max} - V_{recirc})/2$, and K is a coefficient deriving from the assumption of a constant eddy viscosity $\nu_T = (x - x_1)V_1/(4K^2)$ across the shear layer (Fig. 10a). Eq. (12) is compared with the experimental data in Fig. 10b. Fig. 10b also included the water velocity V_w calculated from the time-averaged total pressure by taking into account the local void fraction and ignoring the static pressure component in the high-velocity region. Comparison between the interfacial velocity V_{int} and liquid-phase velocity V_w showed good agreement, by which the non-slip condition was justified in the high-speed air-water flow. In the surrounding water pool, the void fraction was small and the velocity was negligible, and the total pressure equalled to the static pressure related to the local depth.

The maximum velocity V_{max} decreased in the longitudinal direction as the impinging flow decelerated in the receiving bath (Fig. 10c). The present data showed consistent decay trend with that of Bertola et al. (2017) for similar impact velocities. The penetration depth is the distance over which the maximum interfacial velocity decreased from V_1 to zero at stagnation. The faster deceleration seen in Fig. 10c was in accordance with the observation of a smaller penetration depth for a smaller impact velocity (Clanet and Lasheras, 1997; Harby et al., 2014; Kramer et al., 2016). The change in jet length did not modify the positive velocity distributions significantly for the tested flow conditions. However, for all impact velocities, no upward motion was recorded ($V_{recirc} = 0$) for the smallest jet length $x_1 = 0.05$ m, whereas negative velocities ($V_{recirc} < 0$) were measured on the still-water side of the shear layer for longer jet lengths $x_1 = 0.1$ and 0.15 m. The presence of negative velocity was associated with the rotational motion of large vortical structures in the shear layer, as a form of Kevin-Helmholtz instability, which was enhanced by larger jet disturbance developing over a longer jet falling distance.

The expansion rate of the momentum shear layer is inversely proportional to the coefficient K in Eq. (12). The value of K increased almost linearly with increasing longitudinal distance, as shown in Fig. 10d. The present data compared well with the previous datasets. As the depth increased and the local mean void fraction decreased, the value of K in the air-water plunging jet approached the typical value of $K \sim 11$ for monophase shear layers.

5.2. Turbulence intensity

The cross-sectional profiles of interfacial turbulence intensity Tu_{int} calculated with Eq. (2) are presented in Fig. 11 for two impact velocities with the same jet length. The results are compared to the data of Bertola et al. (2017) at close longitudinal positions. The interfacial turbulence intensity results were typically at a high level from 0.5 up to 3–4, increasing slightly with increasing impact velocity and decreasing in the longitudinal direction. The very-high

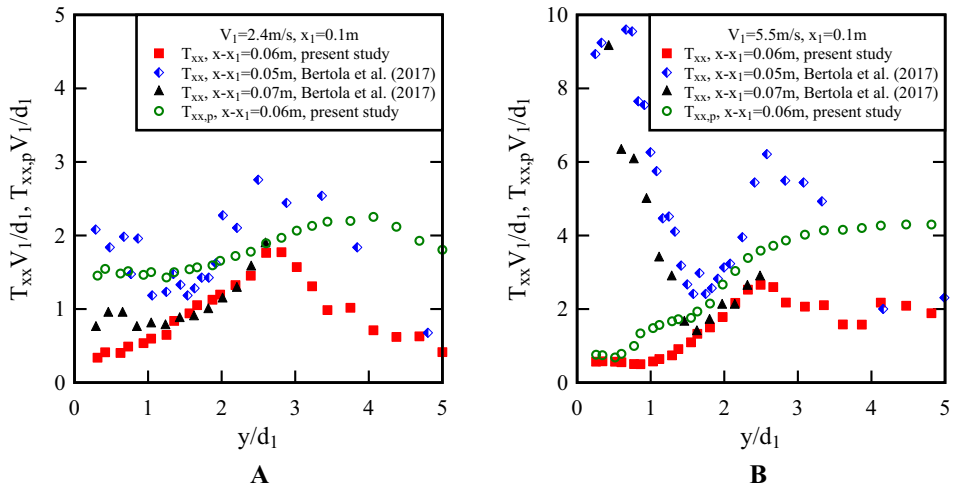

Fig. 12. Auto-correlation time scales of bubbly flow structures and air-water flow total pressure field – Comparison with bubbly flow auto-correlation time scale data of Bertola et al. (2017): (A) $V_1 = 2.4$ m/s, $x_1 = 0.1$ m; (B) $V_1 = 5.5$ m/s, $x_1 = 0.1$ m.

turbulence intensity reflected the existence of non-randomness in bubble distribution because of the bubble-turbulence interplay, e.g., in a form of bubble clustering, which biased (flattened) the correlation functions of phase-detection probe signals from a Gaussian distribution (Eq. (2)). An evidence was the presence of local maximum interfacial turbulence intensity in a horizontal cross-section corresponding to the detection of bubbles advected in large eddies in the shear layer (Fig. 11b). Sometimes physically-meaningless large values were obtained due to the presence of large-scale flow instabilities such as the oscillations of shear layer position, fluctuations of free-surface elevation, and spanwise movement of three-dimensional jet disturbance structures. This can be seen in the previous Tu_{int} data of Bertola et al. (2017) between $y/d_1 = 0$ and 1.5 (Fig. 11b). These extremely large values were believed to link with the formation of jet disturbance structures against the jet support boundary and the associated entrainment of air cavities between the jet and the wall, at a time scale significantly greater than the turbulence time scale in bubble advection. For comparison, the reduction of jet disturbance in the present experimental setup yielded much meaningful turbulence intensity data.

In Fig. 11, the interfacial turbulence intensity Tu_{int} is further compared with the water-phase turbulence intensity Tu_w deriving from the total pressure data. Both approaches (Eqs. (5) and (6)) were applied. Similar results were obtained between the two approaches with an error typically less than 15%. In some flow regions with relatively high void fraction and low velocity, the PDF of total pressure samples did not show well-separated bimodal distributions as in Fig. 3, and we assumed $\alpha = C$ for Eq. (5) for the approximate of Tu_w in this case. Fig. 11 shows water-phase turbulence intensities in the order of 10^{-1} in the jet core (e.g. $0 < y/d_1 < 1.5$ in Fig. 11 at $x - x_1 = 0.06$ m, for both impact velocities), which increased slightly in the shear layer (e.g. $y/d_1 > 1.5$ in Fig. 11). The water-phase turbulence intensity Tu_w was typically one order of magnitude smaller than the interfacial turbulence intensity Tu_{int}, suggesting considerable difference between the two quantities. Further, one must be careful with the respective assumptions for the use of Eqs. (2), (5) and (6) as well as the associated uncertainties for the estimate of turbulence intensities in a highly-turbulent bubbly flow.

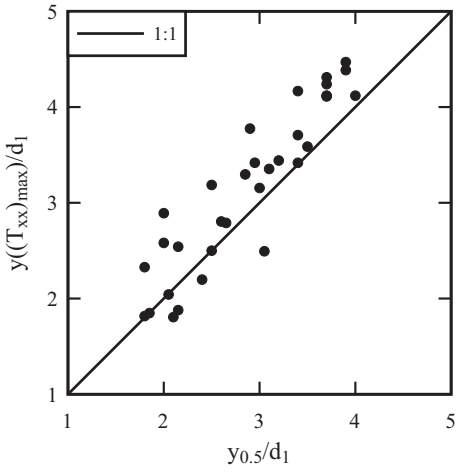

Fig. 13. Characteristic positions of maximum auto-correlation time scales and maximum time-averaged velocity gradient – 2.4 m/s < V_1 < 5.6 m/s, 0.05 m < x_1 < 0.15 m, 0.03 m < $x - x_1$ < 0.19 m.

5.3. Turbulence auto-correlation time scale

The auto-correlation time scale of phase-detection probe signal, T_{xx}, defined by Eq. (3), characterised a "lifetime" of the advective bubbly flow structures. Its counterpart of total pressure signal, $T_{xx,p}$, was also calculated. Typical results are presented in Fig. 12 and compared with the bubbly flow time scale reported by Bertola et al. (2017). It is noteworthy that, unlike the water-phase turbulence intensity Tu_w, the total pressure auto-correlation time scale $T_{xx,p}$ was directly derived from the total pressure signal and consisted of both contributions of water-phase flow and bubbly flow structures detected by the total pressure sensor. Therefore, the data $T_{xx,p}$ was expected qualitatively larger than T_{xx}, as proofed by the experimental results in Fig. 12. Similar to the comparison of interfacial turbulence intensity Tu_{int} between the present work and Bertola et al. (2017) (Fig. 11), the previous auto-correlation time scale data was extremely high next to the jet support ($0 < y/d_1 < 1.5$) because of the large-scale unsteady flow motions in the form of longitudinal propagation

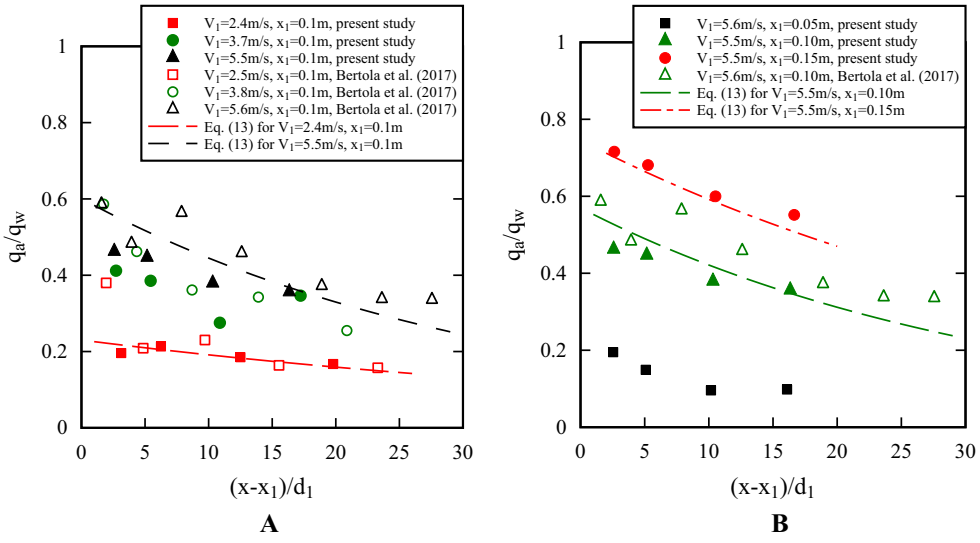

Fig. 14. Longitudinal variation of air entrainment rate in plunging pool, with comparison to data of Bertola et al. (2017): (A) Effects of impact velocity for given jet length x_1 = 0.1 m; (B) Effects of jet length for given impact velocity V_1 = 5.5–5.6 m/s.

and transverse movement of three-dimensional disturbance structures.

In a given cross-section, the bubbly flow auto-correlation time scale T_{xx} exhibited a maximum value in the shear flow where large-size vortical structures interacted intensively with bubbles. The bubbly vortex maintained its coherent structure over a relatively long distance when advected downward in the shear layer, yielding a relatively large turbulent time scale. The magnitude of dimensionless maximum auto-correlation time scale $(T_{xx})_{max}V_1/d_1$ ranged from 0.001 to 0.005, independent of the depth and increasing with either increasing impact velocity or increasing jet length. The position of the maximum time scale $y((T_{xx})_{max})$ was found close to the characteristic position $y_{0.5}$ in Eq. (12), as demonstrated by Fig. 13. The position $y_{0.5}$ was where the time-averaged velocity gradient was maximum. Beyond this position with increasing distance from the jet support, the total pressure auto-correlation time scale $T_{xx,p}$ reached a higher level, because the large time scale of free-surface fluctuations became overwhelming when the kinetic pressure in surrounding water was negligible.

6. Air entrainment rate

The air entrainment in a plunging jet consisted of the pre-aeration in the impinging jet and the singular air entrainment at the impingement point. The air flux in the subsurface air-water flow region was calculated in the form of Eq. (8), with the upper limit of integral being the position of zero time-averaged velocity. That is, the air flux q_a was integrated across the positive velocity region. The air entrainment rate, namely the ratio of entrained air flux to water discharge q_a/q_w, is presented in Fig. 14 for selected flow conditions, to demonstrate the effects of impact velocity (Fig. 14a) and jet length (Fig. 14b) on its longitudinal evolution. The data of Bertola et al. (2017) are included for comparison.

For all tested flow conditions, the results showed a wide range of air entrainment rate from $q_a/q_w = 0.05$ to 0.8 for different impact velocities and jet lengths at immediately below the impingement point. The air entrainment capacity of plunging jet was significantly enhanced by either increasing the impact velocity or elongating the jet length. Despite some data scatter due to the velocity measurement uncertainties, the present air entrainment rate data showed generally a decreasing trend with increasing depth, especially for large impact velocities. This was consistent with the finding of Bertola et al. (2017). The longitudinal decreasing air flux distribution in the near-field of impingement point was believed to link with the relatively high jet disturbance level. At large jet impact velocities, the high initial air flux at the impingement point and the following rapid decay between $x - x_1 = 0$ and $\sim 10d_1$ corresponded to a detrainment of the air bubbles entrapped by the breaking jet surface and the fluctuating free-surface of the receiving pool. These bubbles were not advected into deep water because of their low momentum against the recirculating current and buoyancy. The rate of detrainment became small further downstream $(15 < (x - x_1)/d_1 < 25)$, yielding relatively constant air flux levels. For small impact velocities, constant air entrainment rate was seen for $0 < (x - x_1)/d_1 < 25$, similar to the finding of little longitudinal detrainment reported by Brattberg and Chanson (1998) albeit for a much wider range of jet velocities with lower jet disturbance. Overall, the longitudinal evolution of near-field air entrainment rate could be fitted with an exponential law:

$$\frac{q_a}{q_w} = \alpha \exp\left(-\beta \frac{x - x_1}{d_1}\right) \tag{13}$$

with the coefficients α and β as functions of the jet flow conditions. Along with the present data and the data of Bertola et al. (2017), α and β were correlated to the dimensionless impact velocity (2.4 m/s < V_1 < 7.4 m/s) and jet length (0.05 m < x_1 < 0.15 m):

$$\alpha = 0.043 \frac{V_1}{\sqrt{g d_1}} + 0.030 \frac{x_1}{d_1} - 0.37 \tag{14}$$

$$\beta = 0.00125 \frac{V_1}{\sqrt{g d_1}} - 0.00154 \frac{x_1}{d_1} + 0.0229 \tag{15}$$

Eq. (13) is compared with the experimental data in Fig. 14 for given flow conditions. Its prediction for all investigated flow conditions is plotted in Fig. 15 against the physical data, showing satisfactory agreement for most conditions. It is noteworthy that, though differences in air entrainment rate were observed between the present and previous studies because of different jet distur-

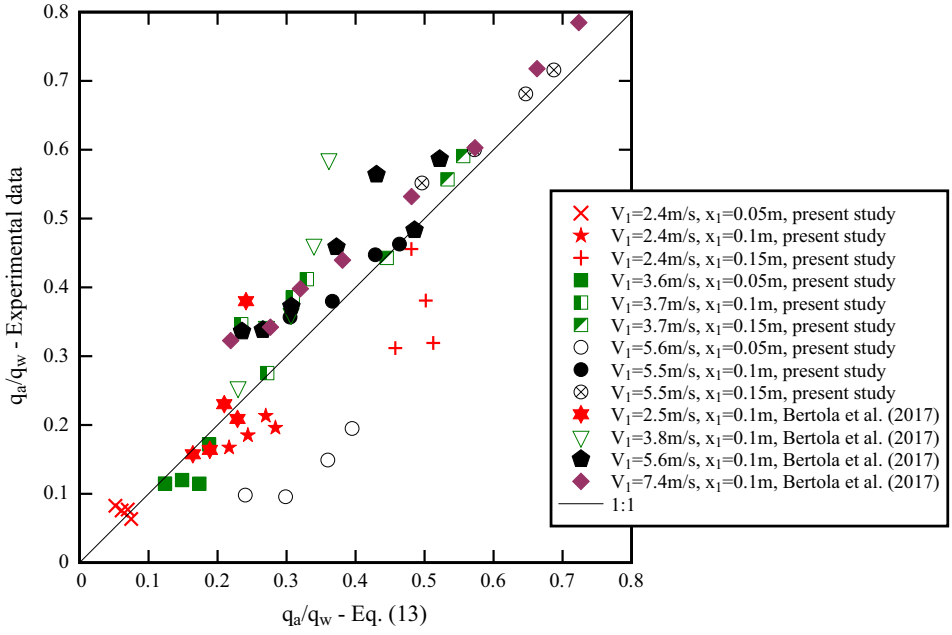

Fig. 15. Comparison of air entrainment rate between experimental data and calculation by empirical law (Eq. (13)).

bance levels (Fig. 14), the effects of jet disturbance were not quantified in Eqs. (14) and (15) with current limited physical data in the literature.

The air entrainment in the investigated plunging jet was characterised by a substantial contribution of pre-entrainment in the jet, including occasionally additional air entrainment between the jet and support wall associated with the jet instabilities. The proportion of pre-entrainment contribution was found typically between 45% and 70% in the present study, higher for small entrainment rates and lower for large entrainment rates. This proportion range was higher than the range of 23–47% observed in Bertola et al. (2017). Nevertheless, both studies indicated that, for a plunging jet with highly turbulent inflow conditions, the jet pre-aeration could be equally important as the air entrainment at the jet impingement, thus should not be ignored.

7. Conclusion

A physical study was performed to investigate the air-water flow properties and bubble-turbulence interplay in vertical planar supported plunging jets. The air-water flow properties and total pressure were measured in both falling jet and plunging pool. A combination of three impact velocities and three jet lengths were investigated. For the same impact velocity, a longer jet corresponded to more developed jet disturbances at the impingement.

The impinging jet was characterised by substantial free-surface air entrainment, with a rapid increase in air flux and surface mixing layer thickness along the jet. Some large disturbance was observed for large jet velocities and jet lengths, leading to additional air entrainment from occasionally-formed air cavities between the jet and support walls. Quantification of free-stream turbulence intensity was possible in the highly-aerated jet based on total pressure measurement. Eliminating the bubble impact from total pressure samples, the jet turbulence intensity was estimated to be about 0.05. The installation of in-pipe flow redistributors upstream of the jet nozzle reduced the jet disturbance and instabilities, while it slightly increased the free-stream turbulence intensity.

The time-averaged void fraction and bubble count rate distributions in the downstream vicinity of impingement point were affected by the pre-entrainment in the jet. The downward bubble transport was primarily an advective diffusion process, and the void fraction profiles followed the analytical solution of point-source bubble diffusion equation. For most flow conditions, the cross-sectional average bubble diffusivity increased with increasing depth as the bubble diffusion layer broadened. However, with a significant jet disturbance, high bubble diffusivity was observed immediately below the impingement point, and it decreased to the same level of $D_t \sim 0.07$ in deep water as for less disturbing inflow conditions. Both maximum void fraction and maximum bubble count rate increased with increasing impact velocity and increasing jet length, and their positions did not coincide. The turbulence modification and surface breaking in the jet led to large bubble count rate at the impingement point and a monotonic longitudinal decrease in the corresponding Strouhal number, differing from the dominant process of large entrained air packets breaking into small bubbles for unmodified jet conditions.

The longitudinal velocity, turbulence intensity and auto-correlation time scale were derived from both phase-detection probe signal and total pressure signal, separately. Ignoring the static pressure in high-velocity regions, the two instruments gave close interfacial velocity and water-phase velocity. A variation in jet length did not change the longitudinal deceleration rate for the same impact velocity, but the flow reversal was enhanced with a longer jet. The expansion rate of the shear layer was enlarged by the presence of air bubbles and decreased as the flow de-aerated. Remarkable difference was shown between the interfacial and water-phase turbulence intensities. Any estimate of turbulence properties involving correlation analyses could be sensitive to the presence of large-scale turbulence and flow instabilities, and the turbulence level in the affected region might be overestimated. The bubbly-flow auto-correlation time scale showed a maximum at the position of greatest velocity gradient, implying that the bubbly flow maintained its coherent eddy structures for a longer time in the shear layer as well as for a larger impact velocity or a longer jet length. The longitudinal detrainment rate in the near-field could be modelled by an empirical exponential law as a function of the jet velocity and falling height for a range of flow conditions. The air entrainment rate data highlighted the pre-entrainment contribution.

Overall, the jet impact velocity and jet length had significant effects on the air entrainment and subsurface air-water flow properties in plunging jets. A larger jet impact velocity or a longer jet length increased the air content, air-water interfacial area, air entrainment rate and mean bubble size in the plunging pool. The impact of jet disturbance was mainly observed within a short distance below the impingement point, in terms of bubble population, diffusivity and detrainment. A correlation analysis could provide indicators of large-scale disturbance. Both levels of inflow turbulence and disturbance affected the air entrainment capacity of plunging jets and potentially the mass/heat transfer, thus should be carefully evaluated when the air-water flow is of primary concern.

Acknowledgement

The authors thank Jason Van Der Gevel (The University of Queensland) for laboratory technical support. The research is funded by Australian Research Council (Grant DP120100481). The second author is sponsored by Indonesia Endowment Fund for Education.

References

Bertola, N.J., Wang, H., Chanson, H., 2017. Air bubble entrainment at vertical plunging jets: a large-scale experimental study. Hydraulic Model Report No. CH104/17, School of Civil Engineering, The University of Queensland, Brisbane, Australia, 256 pages.

Bin, A., 1993. Gas entrainment by plunging liquid jets. Chem. Eng. Sci. 48 (21), 3585–3630.

Brattberg, T., Chanson, H., 1998. Air entrapment and air bubble dispersion at two-dimensional plunging water jets. Chem. Eng. Sci. 53 (24), 4113–4127.

Brattberg, T., Chanson, H., Toombes, L., 1998. Experimental investigations of free-surface aeration in the developing flow of two-dimensional water jets. J. Fluid Eng., Trans. ASME 120 (4), 738–744.

Chirichella, D., Gomez Ledesma, R., Kiger, K.T., Duncan, J.H., 2002. Incipient air entrainment in a translating axisymmetric plunging laminar jet. Phys. Fluids 14, 781–790.

Chanson, H., 1997. Air Bubble Entrainment in Free-surface Turbulent Shear Flows. Academic Press, London, UK. 401 pages.

Chanson, H., 2009. Turbulent air-water flows in hydraulic structures: dynamic similarity and scale effects. Environ. Fluid Mech. 9 (2), 125–142. https://doi.org/10.1007/s10652-008-9078-3.

Chanson, H., Carosi, G., 2007. Advanced post-processing and correlation analyses in high-velocity air-water flows. Environ. Fluid Mech. 7 (6), 495–508.

Chanson, H., Manasseh, R., 2003. Air entrainment processes in a circular plunging jet. Void fraction and acoustic measurements. J. Fluid Eng., Trans. ASME 125 (5), 910–921. https://doi.org/10.1115/1.1595672.

Clanet, C., Lasheras, J.C., 1997. Depth of penetration of bubbles entrained by a plunging water jet. Phys. Fluids 9 (7), 1864–1866.

Crowe, C., Sommerfield, M., Tsuji, Y., 1998. Multiphase Flows with Droplets and Particles. CRC Press, Boca Raton, USA. 471 pages.

Cummings, P.D., Chanson, H., 1997a. Air entrainment in the developing flow region of plunging jets – part 1: theoretical development. J. Fluid Eng., Trans. ASME 119 (3), 597–602.

Cummings, P.D., Chanson, H., 1997b. Air entrainment in the developing flow region of plunging jets – part 2: experimental. J. Fluid Eng., Trans. ASME 119 (3), 603–608.

Cummings, P.D., Chanson, H., 1999. An experimental study of individual air bubble entrainment at a planar plunging jet. Chem. Eng. Res. Design, Trans. IChemE Part A 77 (A2), 159–164.
Ervine, D.A., McKeogh, E.J., Elsawy, E.M., 1980. Effect of turbulence intensity on the rate of air entrainment by plunging water jets. Proc. Inst. Civ. Eng. Part 2, 425–445.
Felder, S., Chanson, H., 2014. Triple decomposition technique in air–water flows: application to instationary flows on a stepped spillway. Int. J. Multiph. Flow 58, 139–153. https://doi.org/10.1016/j.ijmultiphaseflow.2013.09.006.
Harby, K., Chiva, S., Muñoz-Cobo, J.L., 2014. An experimental study on bubble entrainment and flow characteristics of vertical plunging water jets. Exp. Therm Fluid Sci. 57, 207–220.
Hoyt, J.W., Taylor, J.J., 1977. Waves on water jets. J. Fluid Mech. 83 (1), 119–127.
Kiger, K., Duncan, J., 2012. Air-entrainment mechanisms in plunging jets and breaking waves. Annu. Rev. Fluid Mech. 44, 563–596.
Kirchner, W.G., 1974. Gas entrainment by plunging liquid jets. In: Proceedings of 5th Australasian Conference on Hydraulics and Fluid Mechanics, 9–13 Dec, Christchurch, New Zealand.
Kramer, M., Wieprecht, S., Terheiden, K., 2016. Penetration depth of plunging liquid jets – a data driven modelling approach. Exp. Therm Fluid Sci. 76, 109–117.
Lin, T.J., Donnelly, H.G., 1966. Gas bubble entrainment by plunging laminar liquid jets. AIChE Jl. 12 (3), 563–571.
Low, H.S., 1986. Model studies of Clyde dam spillway aerators Research Report No. 86-6. Dept. of Civil Eng., Univ. of Canterbury, Christchurch, New Zealand.
McKeogh, E.J., Ervine, D.A., 1981. Air entrainment rate and diffusion pattern of plunging liquid jets. Chem. Eng. Sci. 36, 1161–1172.
Mudde, R.F., 2005. Gravity-driven bubbly flows. Annu. Rev. Fluid Mech. 37, 393–423.
Qu, X.L., Khezzar, L., Danciu, D., Labois, M., Lakehal, M., 2011. Characterization of plunging liquid jets: a combined experimental and numerical investigation. Intl. J. Multiph. Flow 37 (7), 722–731.
Rajaratnam, N., 1976. Turbulent Jet. Development in Water Science, vol. 5. Elsevier Scientific Publishing Company, New York, USA.
Schlichting, H., 1979. Boundary Layer Theory. McGraw-Hill, New York, USA. 800 pages.
Sene, K.J., 1988. Air entrainment by plunging jets. Chem. Eng. Sci. 43 (10), 2615–2623.
Serizawa, A., Kataoka, I., Michiyoshi, I., 1975. Turbulence structure of air-water bubbly flow – I. Measuring techniques. Int. J. Multiph. Flow 2, 221–233.
Soh, W., Khoo, B., Yuen, W., 2005. The entrainment of air by water jet impinging on a free surface. Exp. Fluids 39 (3), 498–506. https://doi.org/10.1007/s00348-005-0965-9.
Thomas, N.H., Auton, T.R., Sene, K., Hunt, J.C.R., 1983. Entrapment and transport of bubbles by transient large eddies in multiphase turbulent shear flows. In: Proc. Intl. Conf. on Physical Modelling of Multiphase Flow, BHRA Fluid Eng., Coventry, UK, pp. 169–184.
Toombes, L., 2002. Experimental study of air-water flow properties on low-gradient stepped cascades Ph.D. thesis. Dept. of Civil Engineering, The University of Queensland, Brisbane, Australia.
Van De Donk, J., 1981. Water aeration with plunging jets Ph.D. thesis. TH Delft, The Netherlands. 168 pages.
Wang, H., Felder, S., Chanson, H., 2014. An experimental study of turbulent two-phase flow in hydraulic jumps and application of a triple decomposition technique. Exp. Fluids 55 (7). https://doi.org/10.1007/s00348-014-1775-8. 18 pages.
Wang, H., Chanson, H., 2016. Self-similarity and scale effects in physical modelling of hydraulic jump roller dynamics, air entrainment and turbulent scales. Environ. Fluid Mech. 16 (6), 1087–1110. https://doi.org/10.1007/s10652-016-9466-z.
Zhang, G., Chanson, H., Wang, H., 2016. Total pressure fluctuations and two-phase flow turbulence in self-aerated stepped chute flows. Flow Meas. Instrum. 51, 8–20. https://doi.org/10.1016/j.flowmeasinst.2016.08.007.